

In situ observation of collective grain-scale mechanics in Mg and Mg–rare earth alloys

F. Wang¹, S. Sandlöbes^{*}, M. Diehl, L. Sharma, F. Roters, D. Raabe

Max-Planck-Institut für Eisenforschung, Department for Microstructure Physics and Alloy Design, Max-Planck-Str. 1, Düsseldorf, Germany

Received 13 May 2014; received in revised form 18 July 2014; accepted 22 July 2014

Abstract

The microstructure evolution of pure Mg and two Mg–rare-earth alloys (Mg–3 wt.% Dy and Mg–3 wt.% Er) was studied during in situ compression tests by electron backscatter diffraction and electron channelling contrast imaging. Strain localization and the formation of an early stage shear band (“pre-shear band”) were observed in pure Mg during compressive deformation below 5% engineering strain. In the experiments percolative grain clusters with prevalent basal slip as a precursor for shear band formation was observed. This collective grain-cluster shear behaviour was analysed in more detail using crystal plasticity simulations, revealing a percolation of intense basal slip activity across grain boundaries as the mechanism for shear band initiation. Plane trace analysis, Schmid factor calculation and deformation transfer analysis at the grain boundaries were performed for the activated twins. It appears that many activated tension twins exhibit pronounced non-Schmid behaviour. Twinning appears to be a process of accommodating local strain rather than a response to macroscopic strain.

© 2014 Acta Materialia Inc. Published by Elsevier Ltd. All rights reserved.

Keywords: Magnesium; Shear banding; Deformation twinning; Electron channelling contrast imaging; Crystal plasticity modelling

1. Introduction

Magnesium has a low mass density of 1.74 g cm^{-3} and is the lightest structural metal [1]. Magnesium and its alloys have received great attention for potential use in automotive applications [2]. However, the application of wrought magnesium alloys is restricted by its poor formability at ambient temperatures caused by its strong basal-type texture developed during processing and the lack of available deformation mechanisms [3].

The primary deformation modes at room temperature in magnesium and magnesium alloys are basal slip and $\{10\bar{1}2\}$ tension twinning. Both are easy to activate and

have critical resolved shear stress (CRSS) values of a few MPa according to single crystal experiments [4]. The prevalence of basal dislocation slip produces a fiber texture where the basal planes are closely aligned with the primary material flow direction, limiting the contribution of the basal slip system to further deformation [5,6].

Besides non-basal dislocation slip, twinning can accommodate strain along the crystal *c*-axis, providing additional degrees of freedom matching the requirement for five independent shear systems in the classical Taylor–Bishop–Hill sense [7,8]. However, it was earlier observed via a joint experimental-simulation grain scale micromechanical analysis [9] that if the Taylor–Bishop–Hill criterion is not fulfilled everywhere at the grain scale, collective deformation of grain clusters can in certain cases provide a sufficient number of shear degrees of freedom for compatible polycrystalline deformation [10]. Due to the limitation of available deformation systems, plastic heterogeneities and strain

^{*} Corresponding author.

E-mail address: s.sandloebes@mpie.de (S. Sandlöbes).

¹ Current address: University of Virginia, Materials Science and Engineering, Charlottesville, VA, USA.

localization in the form of shear bands [11] occur during room temperature deformation of Mg [12–18]. The mechanisms associated with such shear band formation in Mg alloys are not well understood [12–18]; some studies suggest $10\bar{1}1$ compression twinning [12,14], double-twinning [14,18], tension twinning [13] or rotational recrystallization [17] as possible mechanisms of shear band formation. Shear banding in Mg is a mesoscopic “grain-cluster” deformation process where the grains inside the shear band are reported to subsequently re-orient in the macroscopic shear direction, i.e. “soften” the sheared region with respect to further basal dislocation slip during continuing deformation [15,17,18].

Similarly, it is well known that twins appear also in grains not suitably oriented for twinning. This anomalous twinning or, more specifically, non-Schmid behaviour of twinning was observed in rolled sheets and extruded Mg alloys, e.g. Refs. [19–23]. With the non-Schmid behaviour of twin variant selection we refer to the fact that the micro-mechanical i.e. the local stress state may profoundly deviate from the macroscopic loading state. It should be noted though that the term non-Schmid behaviour sometimes also refers to the effect of hydrostatic tensor components on plastic flow: this definition is not used here. Apparently, the local microstructure plays an important role in twin activation and topology, besides the dependence on crystallographic orientation or grain size, on which many studies have focused before, e.g. Refs. [23,24]. Grain boundaries are important sites for twin nucleation given that they provide defect sources and stress peaks. The interaction between twinning and grain boundaries was investigated in polycrystalline hexagonal close packed (hcp) Mg and hcp Ti [12,25,26]. It is found that twin nucleation is not solely controlled by Schmid’s law, i.e. a twin variant with a lower Schmid factor might nucleate instead of the expected high Schmid factor twin variant, e.g. Refs. [19–23].

Jonas et al. [22] and Mu et al. [27] suggested that strain accommodation required by the neighbouring grains might influence the variant selection during twinning. The formation of twins involves shearing in the matrix. When a twin nucleates from the grain boundary (GB), the neighbouring grain is also being sheared to accommodate the shape change at the GB [22]. The amount and type of deformation required for strain accommodation in the neighbouring grains then affect which variant is required. Jonas et al. and Mu et al. identified the prismatic $\langle a \rangle$ slip as the critical geometrically necessary deformation system influencing the variant selection of twinning. Capolungo et al. conducted a statistical study of twinning in hcp Zr and showed a strong correlation between twin nucleation and grain boundaries [28]. Grain boundaries are important sites for twin nucleation since they can provide both, crystal defect sources and places of stress concentration [28]. The interaction between primary twins and grain boundaries was described by Christian and Mahajan [29]. They considered that the stress concentration in the vicinity of a

GB–twin intersection can be relaxed either by slip or by slip and twinning in the adjoining grain. El Kadiri et al. [30] found that low angle grain boundaries with misorientations between 13° and 15° are more preferential for tension twin nucleation in Mg than high angle grain boundaries, which actually is another factor influencing non-Schmid twin variant selection.

Barnett et al. [24] ascribed the anomalous formation of non-Schmid oriented secondary twins to a local unloading occurring due to the relative ease of basal $\langle a \rangle$ slip in secondary twins. Additionally, the minimization of compatibility strain of non-Schmid secondary twins to the closest twinning plane of the primary compression twins [24] was assumed to be substantial for variant selection and, particularly, non-Schmid behaviour of secondary twinning [24]. Other authors ascribed the non-Schmid behaviour to the difference between the local and the global stress state [31,32], particularly, strain incompatibility at grain boundaries [31,32].

Twinning stimulated by slip was reported by Wang et al. [26] in pure titanium. They reported strain transfer of prismatic dislocation slip, the primary slip system in hcp Ti, into neighbouring grains as a criterion for the nucleation of tension twins at grain boundaries. Twin pairs at grain boundaries were also observed by Beyerlein et al. [21] and Wang et al. [25]. Their formation was proposed as one twin impacting a GB stimulating the nucleation of another twin in the neighbouring grain, or alternatively, that both twins nucleate mutually at the same location at the GB and grow into their respective parent grains.

Here we focus on studying the activation of plastic heterogeneities such as shear bands and the effects of non-Schmid deformation on tension twinning with specific regard to grain-to-grain interactions and collective grain mechanisms. We performed in situ compression tests on pure Mg and two Mg–rare-earth (Mg–RE) alloys (Mg–3 wt.%Dy and Mg–3 wt.%Er) using electron backscatter diffraction (EBSD) and electron channelling contrast imaging (ECCI) to determine the microstructure evolution and active deformation carriers (dislocations, twins) during deformation. The two Mg–RE alloys were selected due to the texture weakening effects associated with the RE alloying compared to the sharp basal textures in pure Mg [31–36] and to investigate possible effects of RE addition on twinning in Mg alloys [18,37]. Due to high local strains inside and next to shear bands, microstructure characterization using electron microscopy is challenging. Therefore, we applied combined in situ EBSD and ECCI observations on deformed sample surfaces to determine active slip and twinning systems via orientation mapping and slip trace analysis. Additionally we performed crystal plasticity simulations and compatibility analyses of grain-to-grain strain transfer for obtaining insights on the true local micromechanical loading situation and mechanisms associated with the experimentally observed collective grain deformation phenomena. Specifically, we applied crystal plasticity simulations to study the mechanisms leading to the formation of

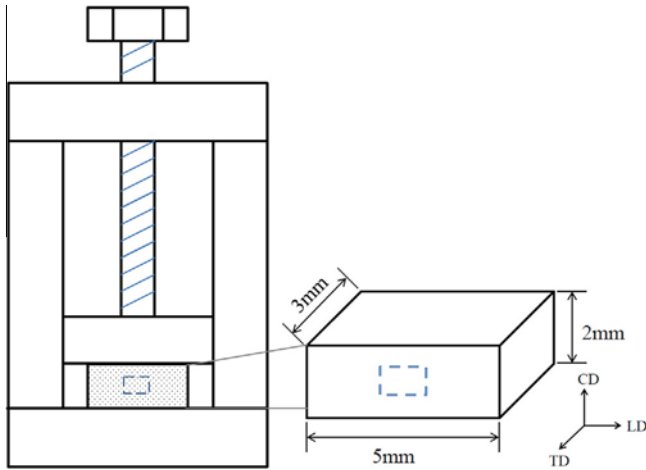


Fig. 1. Schematic sketch of the compression stage, the sample geometry and the sample coordinate system nomenclature. The dashed rectangles illustrate the observation area during in situ compression.

macroscopic shear bands in pure Mg. As dynamic local phenomena such as dislocation pile-ups at grain boundaries are not included in the crystal plasticity framework employed here we used the Luster–Morris parameter (geometric compatibility factor) to analyse the match in grain-to-grain strain transfer.

2. Experimental methods

The alloys were melted and solidified in an induction furnace under Ar pressure (15 bar) in a steel crucible. homogenisation annealing of the as-cast materials was performed for 24 h at 450 °C under Ar atmosphere followed by water quenching. The alloys were hot rolled at 500 °C to a total engineering thickness reduction of 50%, imposing 8–10% reduction per pass. Subsequent recrystallization annealing was carried out at 350 °C under Ar atmosphere for 30 min, again followed by water quenching. Mg–3Er and Mg–3Dy are single hcp phase solid solution alloys. Neither second phases nor severe segregation were observed using electron dispersed X-ray (EDX) analysis.

The in situ specimens were cut via spark erosion to dimensions $5 \times 2 \times 3 \text{ mm}^3$ (longitudinal direction (LD) \times compression direction (CD) \times transverse direction (TD)). The observation planes (CD) were mechanically ground followed by electropolishing using the commercial electrolyte AC2 (Struers). The sample surfaces were preserved during the experiment, which allowed the observation of active deformation systems. Prior to compression the grain orientations were measured by EBSD. In situ compression experiments were carried out in a steel compression stage with displacement control ($\sim 0.002 \text{ mm}$ displacement per compression step, corresponding to 1% strain). Fig. 1 shows a schematic sketch of the compression stage, the sample geometry and the sample coordinate system nomenclature. The samples were kept under load in the compression stage throughout the measurements, and

hence, microstructure relaxation was minimized. Compression was continued until a total strain of $\sim 5\%$; increased surface roughness produced by slip traces and twins after higher deformation inhibits clear ECCI of the microstructures and interferes with Kikuchi pattern indexing. EBSD and ECCI observations were performed on a 1540XB Crossbeam focused ion beam scanning electron microscope at an acceleration voltage of 15 kV [38–40].

3. Deformation analysis methodology

Identification of active deformation systems was conducted by trace analysis in the ECC images combined with orientation data from EBSD, as described in other studies [38–42].

The Schmid factors of the primary deformation systems were calculated under the assumption that the global stress state is uniaxial compression. Twinning differs from slip by its unidirectional nature; i.e. twin shear only proceeds in one direction, which requires the resolved shear stress on the twinning plane to be directed towards the same direction as the shear direction.

3.1. Deformation transfer across the GB

A geometric compatibility factor m' , first defined by Luster and Morris [43], was employed. The group of Bieler and coworkers [25,26,44] successfully applied m' to slip–twin interaction in pure Ti. In the present study, m' was calculated as

$$m' = \cos\varphi \cdot \cos\kappa$$

The angles φ and κ are schematically illustrated in Fig. 2. Since this geometric compatibility is considered for both slip and twinning, the shear direction indicated by “ b ” refers either to the slip direction in the case of dislocations or to shear direction in the case of twinning.

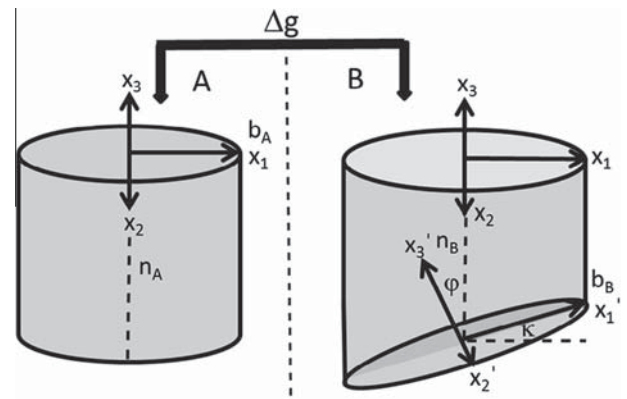


Fig. 2. Geometric alignment of two deformation systems in two neighbouring grains A and B described by angles φ and κ . The two grains are linked by the misorientation matrix Δg . φ is the angle between two plane normals n_A and n_B , and κ the angle between two slip or shear directions b_A and b_B . The figure is reproduced from Ref. [43].

Based on this definition, m' falls in the range $[0, 1]$. A value of $m' = 1$ indicates complete compatibility of the respective deformation systems and a value of $m' = 0$ indicates incompatible deformation across the GB.

Basal slip and tension twinning are considered as primary deformation modes. Non-basal slip systems are assumed improbable to be observed in these experiments for the following reasons:

- (1) Non-basal dislocations cross-slip and cause interaction and network formation inside the microstructure and hence produce only weak wavy slip traces. The associated surface steps are therefore not pronounced.
- (2) The observations were made in large areas at a wide field of view for better statistical relevance but, consequently, with magnifications not high enough to map slip traces of non-basal slip systems.

4. Crystal plasticity modelling

In order to gain more quantitative insights into strain partitioning, local micromechanical stress states and the associated slip system activity, and the mechanisms leading to shear band formation during deformation, crystal plasticity (CP) simulations [45] using a spectral solver [46,47] are conducted. The used CP formulation is a modification of the phenomenological model by Hutchinson [48] for hexagonal crystals incorporated in the DAMASK framework [45,49–51]. The applicability of a similar constitutive model to Mg has been demonstrated by Prakash et al. [52]. In the current formulation, the microstructure is parameterized in terms of a slip resistance s^α ($\alpha = 1, 2, \dots, 18$) on each considered slip system. The following slip systems are incorporated: three basal ($\{0001\}\langle 2-1-10 \rangle$), three first-order prismatic ($\langle a \rangle$ ($\{01-10\}\langle 2-1-10 \rangle$)) six first-order pyramidal ($\langle a \rangle$ ($\{01-11\}\langle 2-1-10 \rangle$)) and six second-order pyramidal ($\langle c+a \rangle$ ($\{2112\}\langle 2-1-13 \rangle$)) systems. These resistances increase asymptotically towards s_∞^α with shears γ^β ($\beta = 1, 2, \dots, 18$) according to the relationship

$$\dot{s}^\alpha = \sum_{\beta=1}^{18} \dot{\gamma}^\beta h_0 \left| 1 - \frac{s^\beta}{s_\infty^\beta} \right|^w \operatorname{sgn} \left(1 - \frac{s^\beta}{s_\infty^\beta} \right) h_{\alpha\beta}$$

with the dislocation interaction matrix ($h_{\alpha\beta}$) and the strain hardening fitting parameters (w, h_0). Given a set of current slip resistances, shear on each system evolves at a rate of

$$\dot{\gamma}^\alpha = \dot{\gamma}_0 \left| \frac{\tau^\alpha}{s^\alpha} \right|^n \operatorname{sgn}(\tau^\alpha)$$

where $\tau^\alpha = \mathbf{S} \cdot (\mathbf{b}^\alpha \otimes \mathbf{n}^\alpha)$ with \mathbf{S} being the external stress tensor and \mathbf{b}^α and \mathbf{n}^α being the unit vectors along the slip directions and slip plane normals, respectively; $\dot{\gamma}_0$ is the reference shear rate and n is the stress exponent. The superposition of shear on all slip systems determines the plastic velocity gradient \mathbf{L}_p :

$$\mathbf{L}_p = \sum_{\beta=1}^{18} \dot{\gamma}^\beta (\mathbf{b}^\beta \otimes \mathbf{n}^\beta)$$

Twinning is introduced in a similar way for the six first-order tension twins (T1) following the concept outlined in Ref. [53].

The constitutive equations are integrated via a full-field spectral CP simulation method [46,47]. This spectral approach is in the current case superior compared to the commonly used finite element method solvers, since it enables one to capture high spatial gradients, cope with pronounced grain-to-grain or in-grain micromechanical contrast and directly use the EBSD measurement points as grid points [46].

The orientation information obtained from the EBSD measurements of the undeformed Mg specimen, shown in Fig. 4, was thus taken as the initial grain-scale patch configuration for the CP simulation. Following Tromans [54] and Agnew et al. [55] the parameters used to model the constitutive response are given in Table 1. As in the experiments, a quasi-static compression loading, namely 10^{-3} s^{-1} , was applied to the microstructural patch until a final average strain of $\sim 5\%$ in the compression direction was reached.

The spectral method employs trigonometric polynomials for the approximation of the posed boundary value problem. Hence, the microstructure is assumed to be periodic. In order to minimize any micromechanical effects stemming from the use of periodic boundary conditions in the model compared to the non-periodic experiments, the simulated microstructure regions are kept larger than those that are being tracked experimentally.

The exact boundary condition tensors used are detailed in Section 6.

5. Experimental results

The deformation microstructures observed during in situ compression are consistent with microstructures observed during bulk ex situ compression. Therefore, we claim that the observed in situ deformation microstructures are representative.

Fig. 3 shows the textures of the initial, recrystallized specimens. The pure Mg specimen exhibits a basal-type texture with a weak texture component which is slightly (a few degrees) tilted towards TD. The Mg–Er and Mg–Dy alloys possess significantly lower basal texture intensities and more scattered texture peaks around (0001). In the case of the Mg–3Er alloy texture components with a sixfold symmetry at $\approx 30^\circ$ from (0001) are present.

5.1. Pure Mg

Fig. 4a–f presents the microstructures observed by ECCI after different compression steps. Additionally, the

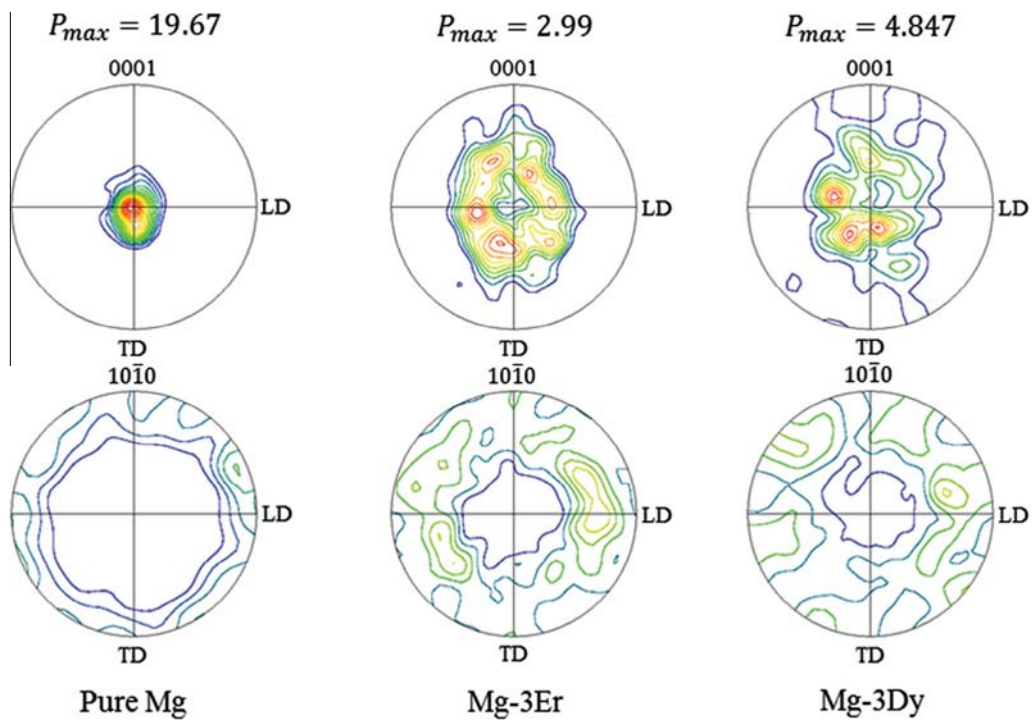


Fig. 3. Initial bulk recrystallization textures of the pure Mg (left), Mg–3Er (middle) and Mg–3Dy (right) samples.

corresponding inverse pole figure (IPF) map (Fig. 4g), kernel average misorientation (KAM) map (Fig. 4h) and image quality (IQ) map with highlighted grain boundaries and twin boundaries (Fig. 4i) after the fifth compression step are shown. After the first and second step (Fig. 4b and c), slip traces appear firstly in the upper part of the observed area. With increasing strain, the slip traces become more distinct and denser, leading to strain localization in the upper part of the region of interest (ROI). Twins are observed after the third compression step, and most of them are of thin lenticular shape. Up to the fifth compression step, all indexed twins in the ROI are tension twins, Fig. 4i. Strain localization and accumulated basal slip activity in the upper half of the ROI are evident from the KAM map and the ECC images.

5.2. Mg–RE alloys

Fig. 5a–e shows the microstructures of the Mg–3Dy sample observed by ECCI after different compression steps, Fig. 5f shows the corresponding IPF map and Fig. 5g the IQ map with highlighted grain boundaries and twin boundaries. After the first step (Fig. 5b), slip traces are homogeneously distributed in many grains in the ROI. Most grains contribute to the overall strain accommodation. With increasing strain, twins are active in many grains and twin propagation is observed. Twin multiplication and activation of different variants are present in some grains (Fig. 5f and g).

The grain-cluster microstructures of the Mg–3Er specimen during compression are shown in Fig. 6. The microstructure development follows a similar trend as observed

for the Mg–3Dy alloy. After the first step (Fig. 6b) only faint slip traces are observed in the ECC image. After the second step (Fig. 6c), slip traces are present in most grains with a similar intensity, respectively. From the third step on, twins were gradually activated in many grains; these twins were indexed as tension twins (Fig. 6h).

In both types of Mg–RE samples, deformation is more homogeneously distributed in the ROIs inspected compared to the pure Mg sample. There is no apparent preference of specific regions or grain orientations where tension twins are activated, while in pure Mg most tension twins are activated inside or adjacent to the strain localization in the upper half of the ROI (Fig. 4).

Compression and secondary twins were observed in the Mg–RE alloys only at higher strains.

5.3. Activation of tension twinning

The observed twins are categorised into four groups: (i) slip stimulated twinning; (ii) twinning stimulated twinning; (iii) twinning originating from triple junctions; and (iv) twinning activated in sample regions below the interaction volume of the sample with the electron beam. We concentrated on categories (i) and (ii) twins in this study due to difficulties in evaluating twin nucleation of categories (iii) and (iv). Twinning as a result of deformation transfer is assessed by employing the Luster–Morris parameter [43], which evaluates the geometric alignment of the deformation modes among abutting grains [44].

Slip stimulated mechanical twinning is determined by the microstructural feature that the “thick end” of a twin at a GB is accompanied by slip traces in the adjacent area

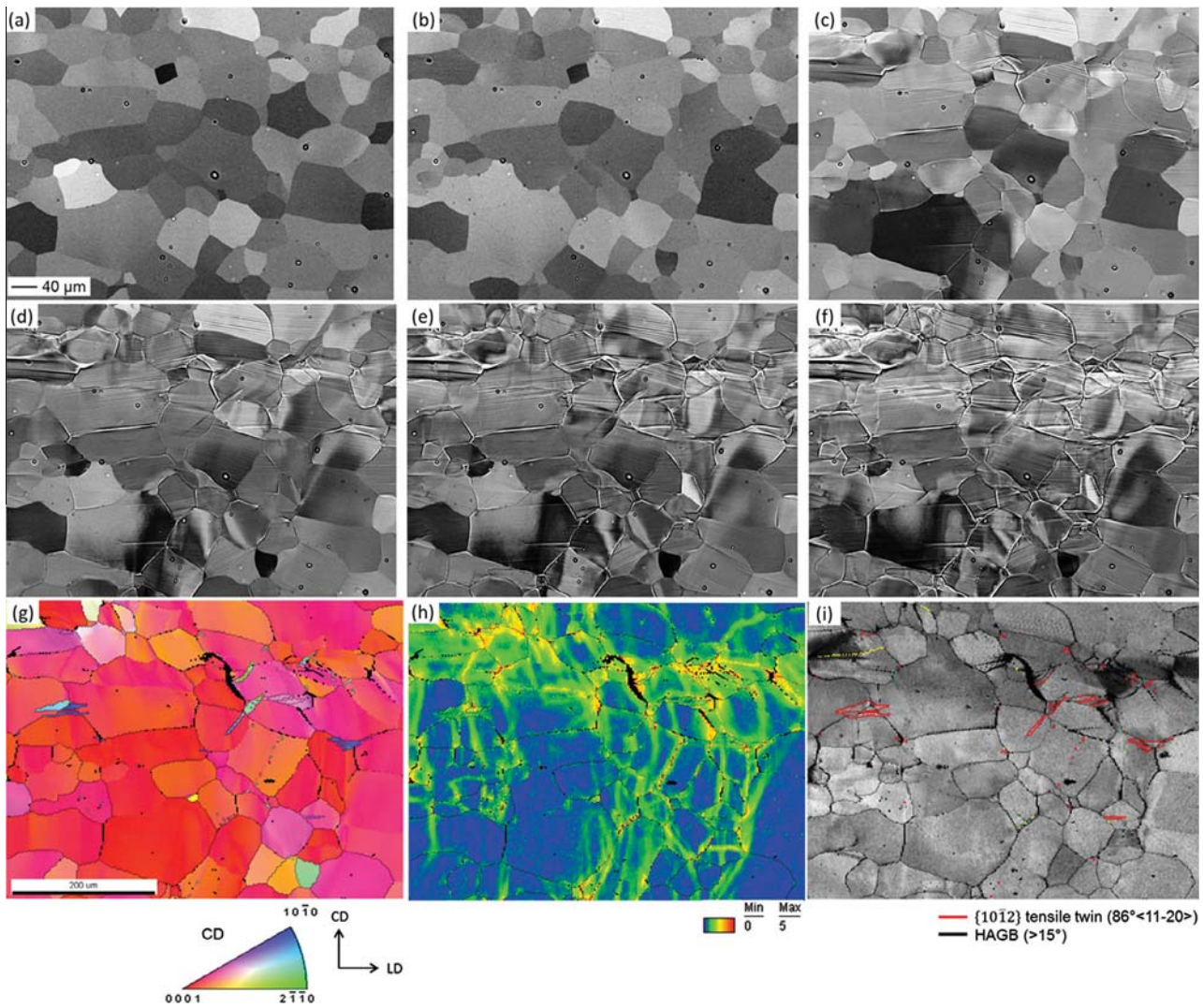


Fig. 4. ECC images of the microstructure development of pure Mg during compression. (a) Microstructure at the initial state without deformation, (b–f) microstructure after the first to the fifth compression step; (g) IPF map, (h) KAM map, (i) IQ map with highlighted grain and twin boundaries of pure Mg after the fifth compression step. Each compression step corresponds to $\sim 1\%$ engineering strain.

Table 1
Material parameters used to model the constitutive response, based on Refs. [54,55].

Property	Value	Unit	Property	Value	Unit	Property	Value	Unit
C_{11}	59.3×10^9	Pa	$s_{0,basal}$	10×10^6	Pa	$s_{0,T1}$	40×10^6	Pa
C_{33}	61.5×10^9	Pa	$s_{\infty,basal}$	40×10^6	Pa	$h_{0,twintwin}$	50×10^6	Pa
C_{44}	16.4×10^9	Pa	$s_{0,prism}$	55×10^6	Pa	$h_{0,twinslip}$	150×10^6	Pa
C_{12}	25.7×10^9	Pa	$s_{\infty,prism}$	135×10^6	Pa			
C_{13}	21.4×10^9	Pa	$s_{0,pyr(a)}$	60×10^6	Pa			
c/a	1.6235	—	$s_{\infty,pyr(a)}$	150×10^6	Pa			
			$s_{0,pyr(c+a)}$	60×10^6	Pa			
			$s_{\infty,pyr(c+a)}$	150×10^6	Pa			
			$h_{0,slipsip}$	500×10^6	Pa			

in the neighbouring grain. Twinning stimulated twinning is determined by two twins meeting at a GB, of which one twin formed first and its impingement on the GB stimulated the nucleation of the other twin. When two twins nucleated during the same compression step at a GB, it cannot be determined if one twin stimulated the nucleation of the other twin or if both twins nucleated simultaneously.

Here, the term “adjoining twin pair” (ATP) [21,56] is adopted to describe this kind of twin.

5.3.1. Pure Mg

In pure Mg twins are commonly formed at and connected with grain boundaries or triple junctions. Fig. 7 shows one region containing such a typical microstructure.

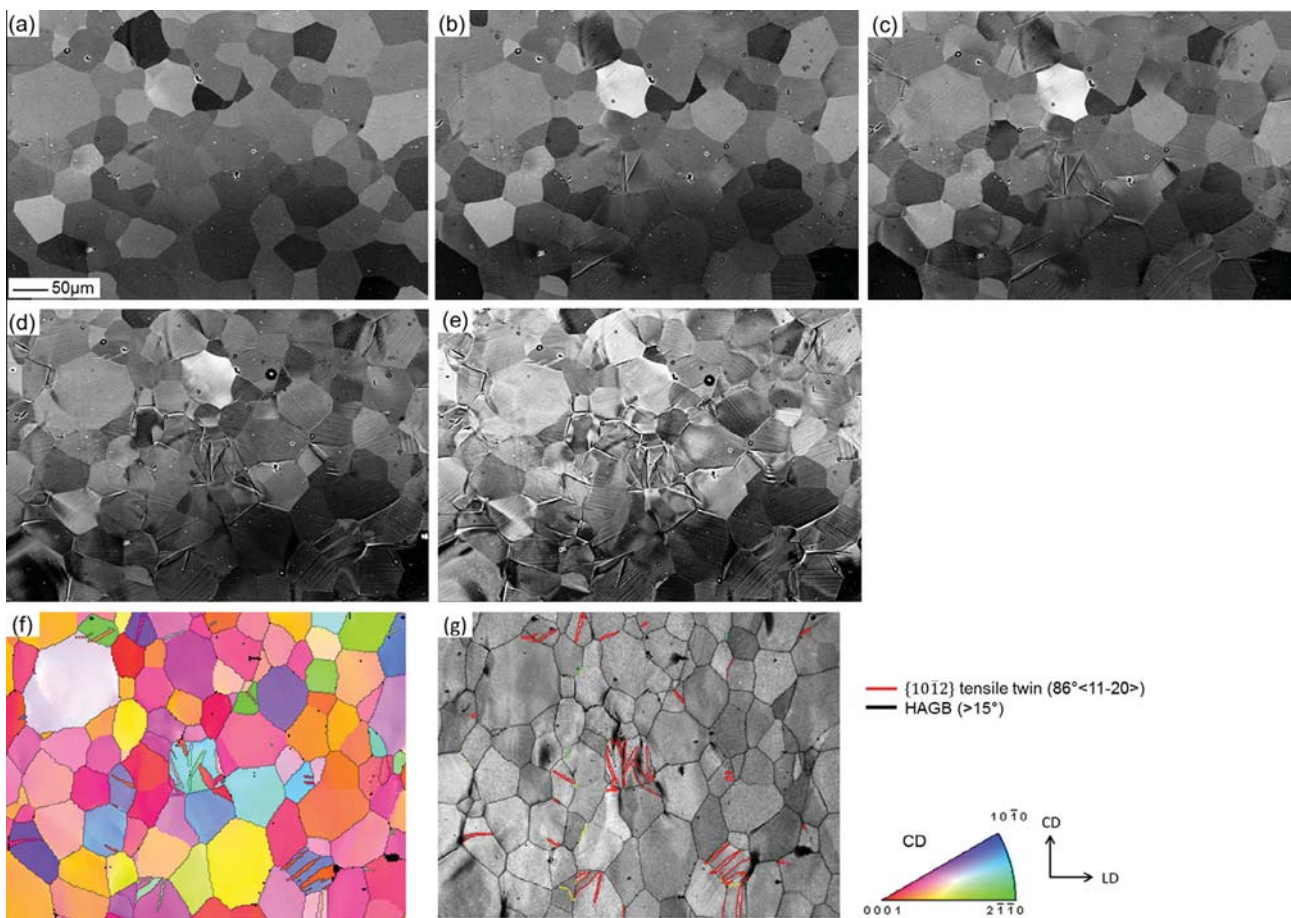


Fig. 5. ECC images of the microstructure development during compression of Mg-3Dy. (a) Microstructure at the initial state without deformation; (b–e) microstructure after the first to the fourth compression steps; (f) IPF map; (g) IQ map with highlighted grain and twin boundaries of Mg-3Dy after the fourth compression step. Each compression step corresponds to $\sim 1\%$ engineering strain.

The twin in grain 7 originated from the triple junction that is formed with grains 6 and 8, as suggested by the thick end at the triple junction and tapering of the twin towards the centre of grain 7. In grain 8, a very fine twin emerged from the GB with grain 5 during the third compression step, and a new twin with the same plane trace inclination (indicated by a white arrow in Fig. 7) emerged from the GB during the fifth compression step. Both twins are accompanied by basal slip traces in grain 5 at the boundary.

Geometric alignment of the basal slip system $(0001)[-1-120]$ in grain 5 and the active twinning system $(1-102)[-1101]$ in grain 8 was analysed, Table 2. All six possible twin variants are of negative Schmid factors m_s with high absolute values. This is not surprising considering the basal texture: grain 8 has its c -axis approximately parallel to the compression direction. The alignment of the observed variant with basal slip in grain 5 is low, as suggested by the very low m' value of 0.084, Table 2. This value suggests that twin formation by strain transfer is very unlikely to occur. As shown in Fig. 7, the observed twin in grain 8 remains thin from the third to the fifth compression step, and no prominent surface steps were formed. This morphology also suggests that operation of this variant is not favoured though it is activated. As a result of the

inability to accommodate strain at the GB via strain transfer, the GB between grains 5 and 8 is of stronger roughness compared to others in the region, i.e. a ledge was produced at the GB. Therefore, the active variant in grain 8 is assumed to have nucleated from this GB as a response to high locally concentrated stress. The twins in the upper part of grain 5 and in grain 6 have one end connected to the triple junction and the other end to the GB. Moreover, both twins are adjoined by a twin in the neighbouring grain at the GB. Each twin of the twin pairs in grains 3 and 5 as well as grains 5 and 6, respectively, emerges during the same compression step (twins in grains 3 and 5 appear after the second step and twins in grains 5 and 6 after the third step), making it difficult to differentiate their sequence of activation. For these adjoining twin pairs, m' values were calculated to assess the geometric alignment between the two systems, Table 3. All twins have negative m_s and high m' values, indicating again the activation of tension twins in pure Mg as a response to the locally concentrated stress.

5.3.2. Mg-RE alloys

Significantly more tension twins are activated in the Mg-RE alloys than in pure Mg; moreover, they are more homogeneously distributed in the microstructure.

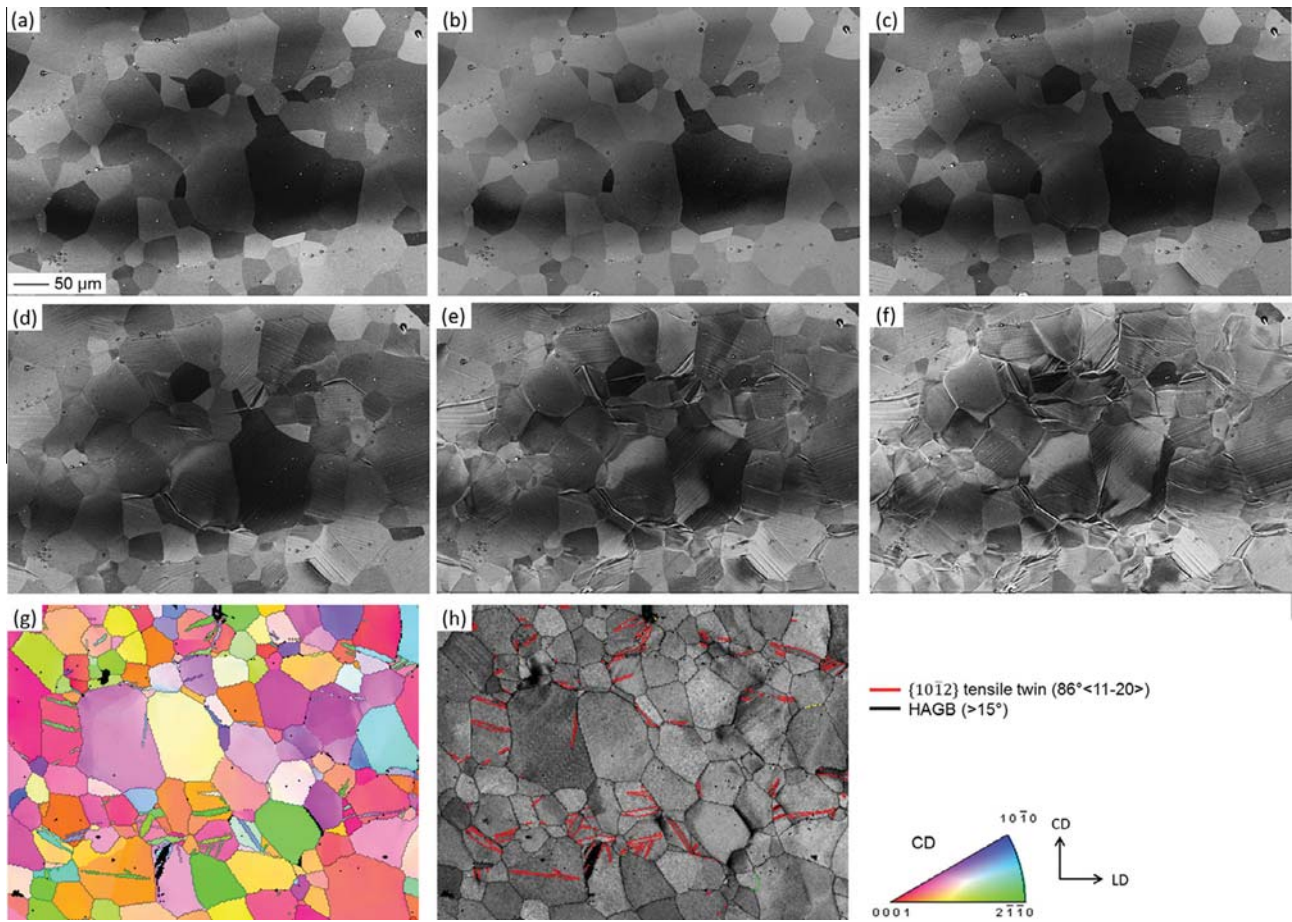


Fig. 6. ECC images of the microstructure development during compression of Mg-3Er: (a) microstructure at the initial state without deformation; (b–f) microstructure from the first to the fifth compression steps; (g) IPF map; (h) IQ map with highlighted grain and twin boundaries of Mg-3Er after the fifth compression step. Each compression step corresponds to $\sim 1\%$ engineering strain.

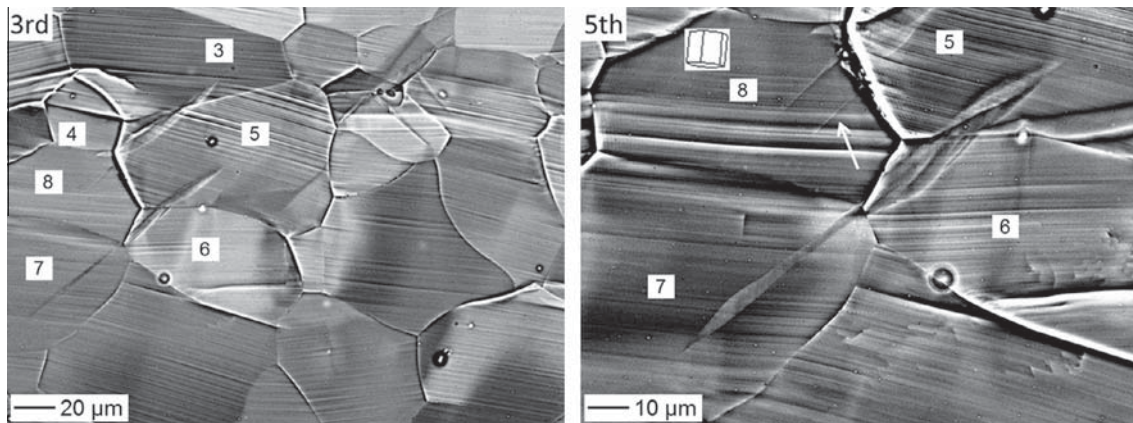


Fig. 7. ECCI of one region in the ROI of the pure Mg sample containing grains 5–8. The left-hand side patch is mapped after the third compression step and the right-hand side patch after the fifth compression step. The hexagonal unit cell in grain 8 illustrates its orientation. Each compression step corresponds to $\sim 1\%$ engineering strain.

Fig. 8 shows slip-induced twinning and twinning-induced twinning in Mg-3Dy. During the second step (Fig. 8b), a very fine twin emerged in grain 2 from the GB with grain 1, as indicated by the arrow. Since the twin is accompanied by slip activity in grain 1 at the GB, its nucleation is attributed to slip stimulation across the GB.

Its highest Schmid factor (0.395) and second highest m' value (0.563) among all six variants confirm the preference of activation, Table 4. During the third step (Fig. 8c), a new twin parallel to the existing one in grain 2 is formed. Additionally, two twins formed in grain 1 with their thick ends meeting the two twins in grain 2 at the GB. Based

Table 2

Geometric analysis of slip and twinning systems in grains 5 and 8 after the third compression step shown in Fig. 7. Schmid factor: m_S ; Luster–Morris parameter: m' ; φ is the angle between two plane normals n_A and n_B , and κ the angle between two slip or shear directions b_A and b_B (see Fig. 2); all angles are specified in degrees.

Grain	Euler angles (φ_1 , ϕ , φ_2)	Slip/twinning systems	m_S	φ	κ	m'
<i>Slip systems in grains 5 and 8</i>						
5	343.2, 63.7, 35.6	(0001)[$\bar{1}\bar{1}20$] ^a	0.386			
8	175.9, 82.8, 164.8	(0001)[$\bar{1}\bar{1}20$] ^a	0.138			
<i>Slip-induced twin in grain 8</i>						
5	343.2, 63.7, 35.6	(0001)[$\bar{1}\bar{1}20$] ^a	0.386			
8	175.9, 82.8, 164.8	($\bar{1}012$)[$10\bar{1}1$]	−0.477	15.0	8.0	0.957
		(01 $\bar{1}2$)[$0\bar{1}11$]	−0.488	87.3	65.1	0.020
		(0 $\bar{1}12$)[$01\bar{1}1$]	−0.470	35.6	40.2	0.621
		(10 $\bar{1}2$)[$\bar{1}011$]	−0.490	78.5	78.8	0.039
		($\bar{1}102$)[$\bar{1}\bar{1}01$]	−0.490	57.6	35.0	0.439
		(1 $\bar{1}02$)[$\bar{1}\bar{1}01$] ^a	−0.486	76.7	68.5	0.084

^a Activated system.

Table 3

Twin pairs in grains 3, 5 and grains 5, 6 in Fig. 7. Schmid factor: m_S ; Luster–Morris parameter: m' .

Grain	m_S	m'
<i>Adjoining twin pairs</i>		
5	−0.313	0.951
3	−0.410	
5	−0.302	0.757
6	−0.447	

on the activation sequence, nucleation of the twins in grain 1 is assumed to be stimulated by the twins in grain 2. The highest m_S (0.275) and m' (0.714) values among the six variants further support this assumption (Table 4). In the following compression steps, twin propagation in length and extension in width are obvious, Fig. 8d.

In addition to basal slip lines covering the whole grain area of grain 1, a set of slip lines with a different inclination is present (Fig. 8e). The new set of plane traces was

identified using EBSD-assisted trace analysis and belongs to the first order pyramidal plane ($\bar{1}101$).

While the active twins in the above-mentioned grains possess the highest Schmid factor and highest Luster–Morris parameter values among all six tension twin variants, it was found that in other grains the observed twins do not always have the highest Schmid factor value. Slip- or twin-induced twins with negative m_S values were frequently observed in both Mg–RE alloys and are, exemplarily, shown in Fig. 9. The twin shown in Fig. 9 is associated with slip in a neighbouring grain with a soft orientation (grains 5 and 9) for basal slip. In grain 4 the active twin variant has a negative m_S and the highest m' value (Table 5a). The last variant in Table 5a has a relatively high Schmid factor, yet it was not activated. In grain 10, while all six twin variants have negative m_S values, suggesting that twin activation is unfavourable with respect to the external compression strain, the one with the highest m' value is observed, Fig. 9 and Table 5b. The Schmid factors

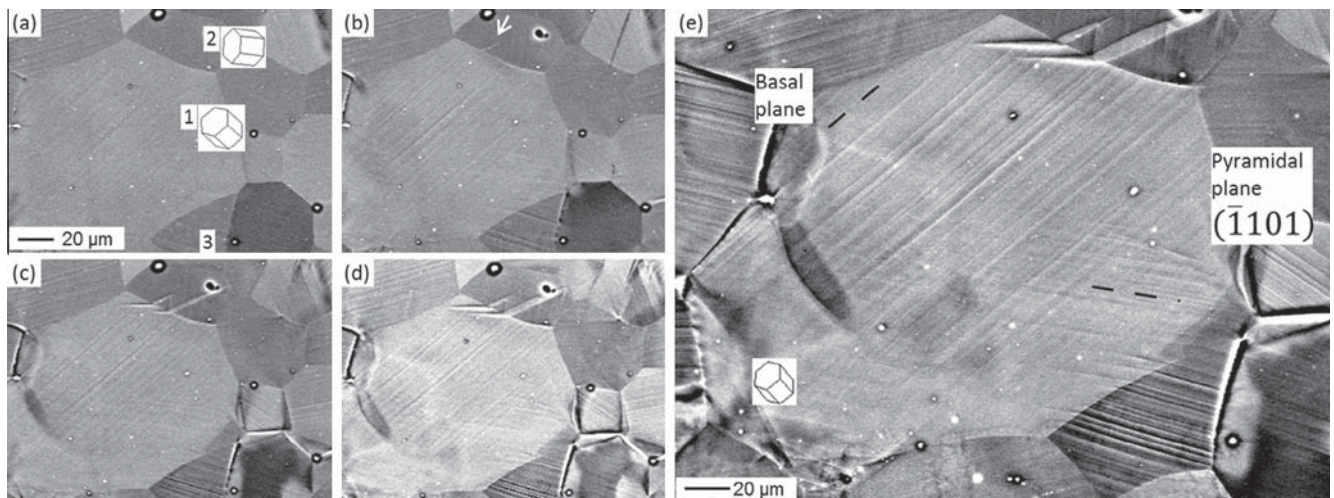


Fig. 8. ECC images showing the microstructure development in one region in the ROI of the Mg–3Dy sample containing grains 1–3. (a–d) are from the first to the fourth compression step. Additional slip lines in grain 1 are illustrated in (e) imaged after the fourth step. Each compression step corresponds to ~1% engineering strain.

Table 4

Deformation transfer at the GB between grains 1 and 2 in Fig. 8. Schmid factor: m_S ; Luster–Morris parameter: m' ; ϕ is the angle between two plane normals n_A and n_B , and κ the angle between two slip or shear directions b_A and b_B (see Fig. 2); all angles are specified in degrees.

Grain	Euler angles (ϕ_1, ϕ, ϕ_2)	Slip/twinning systems	m_S	ϕ	κ	m'
<i>Slip systems in grains 1 and 2</i>						
1	45.1, 44.2, 292.9	(0001)[2 $\bar{1}\bar{1}$ 0] ^a	0.389			
2	82.0, 55.5, 308.2	(0001)[2 $\bar{1}\bar{1}$ 0] ^a	0.084			
<i>Slip-induced twin in grain 2</i>						
1	45.1, 44.2, 292.9	(0001)[2 $\bar{1}\bar{1}$ 0] ^a	0.389			
2	82.0, 55.5, 308.2	($\bar{1}$ 012)[10 $\bar{1}$ 1]	0.341	30.0	42.3	0.641
		(01 $\bar{1}$ 2)[0 $\bar{1}$ 11]	−0.004	83.0	30.9	0.105
		(0 $\bar{1}$ 12)[01 $\bar{1}$ 1]	−0.005	63.5	66.1	0.180
		(10 $\bar{1}$ 2)[$\bar{1}$ 011]	−0.328	57.1	58.5	0.284
		($\bar{1}$ 102)[1 $\bar{1}$ 01] ^a	0.395	54.4	14.7	0.563
		(1 $\bar{1}$ 02)[$\bar{1}$ 101]	−0.382	75.0	72.8	0.077
<i>Twinning-induced twin in grain 1</i>						
2	82.0, 55.5, 308.2	($\bar{1}$ 102)[1 $\bar{1}$ 01] ^a	0.395			
1	45.1, 44.2, 292.9	($\bar{1}$ 012)[10 $\bar{1}$ 1]	0.078	75.7	36.9	0.197
		(01 $\bar{1}$ 2)[0 $\bar{1}$ 11]	−0.074	43.7	38.3	0.567
		(0 $\bar{1}$ 12)[01 $\bar{1}$ 1]	−0.090	65.9	51.2	0.256
		(10 $\bar{1}$ 2)[$\bar{1}$ 011]	−0.041	86.1	52.3	0.042
		($\bar{1}$ 102)[1 $\bar{1}$ 01] ^a	0.275	35.7	28.5	0.714
		(1 $\bar{1}$ 02)[$\bar{1}$ 101]	−0.222	60.2	57.8	0.265

^a Activated system.

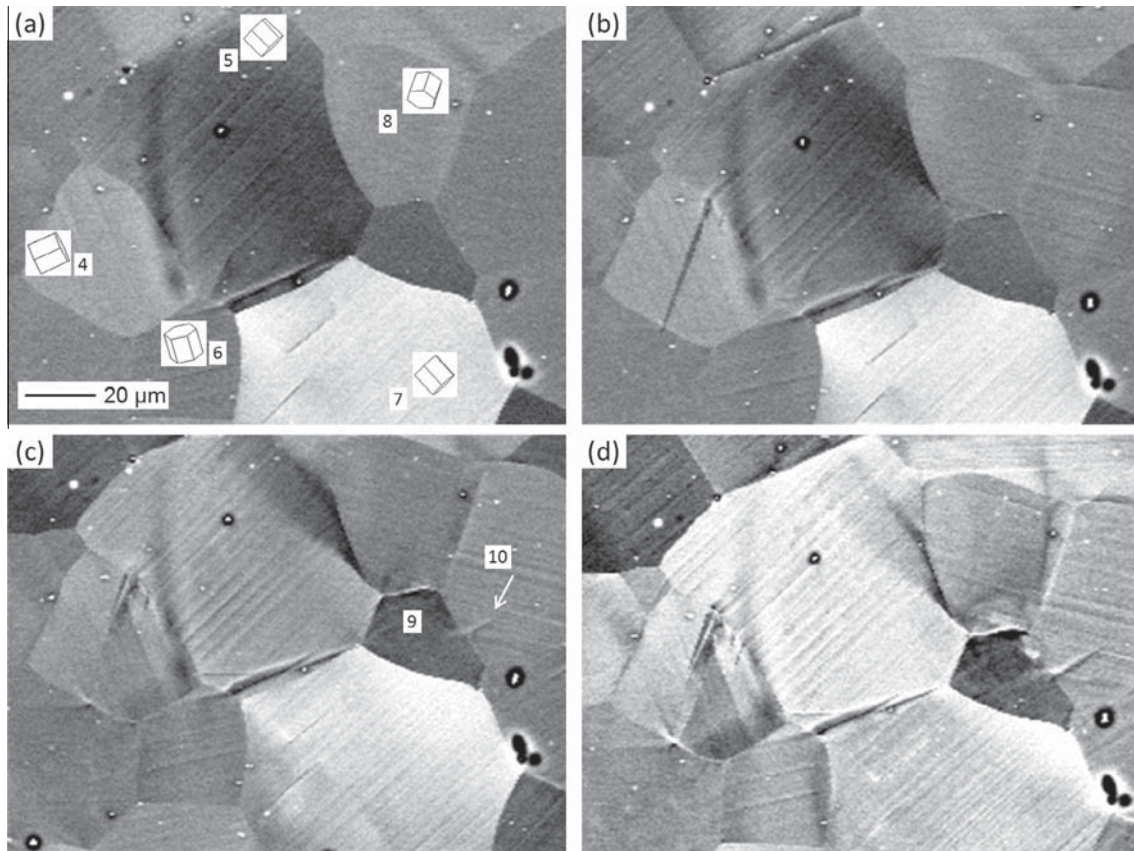


Fig. 9. ECC images showing microstructure development in one region in the ROI of the Mg–3Dy sample containing grains 4–10; (a–d) are from the first to the fourth compression step. The arrow in (c) indicates the twin emerging from the GB. Each compression step corresponds to ~1% engineering strain.

Table 5a

Deformation transfer at the GB between grains 4 and 5 in Fig. 9. Schmid factor: m_s ; Luster–Morris parameter: m' ; φ is the angle between two plane normals n_A and n_B , and κ the angle between two slip or shear directions b_A and b_B (see Fig. 2); all angles are specified in degrees.

Grain	Euler angles ($\varphi_1, \phi, \varphi_2$)	Slip/twinning systems	m_s	φ	κ	m'
<i>Slip systems in grains 4 and 5</i>						
4	222.8, 84.3, 162.3	(0001)[$\bar{1}2\bar{1}0$] ^a	0.330			
5	292.7, 86.0, 89.6	(0001)[$\bar{1}2\bar{1}0$] ^a	0.465			
<i>Slip-induced twin in grain 4</i>						
5	222.8, 84.3, 162.3	(0001)[$\bar{1}2\bar{1}0$] ^a	0.465			
4	292.7, 86.0, 89.6	($\bar{1}012$)[$10\bar{1}1$]	−0.013	61.1	57.8	0.258
		($01\bar{1}2$)[$0\bar{1}11$]	−0.029	19.6	52.1	0.579
		($0\bar{1}12$)[$01\bar{1}1$]	0.052	74.7	83.9	0.028
		($10\bar{1}2$)[$\bar{1}011$]	0.035	43.8	88.6	0.018
		($\bar{1}102$)[$1\bar{1}01$] ^a	−0.328	34.6	26.7	0.735
		($1\bar{1}02$)[$\bar{1}101$]	0.374	67.5	67.3	0.148

^a Activated system.

and the Luster–Morris parameters of the observed tension twins in pure Mg, Mg–3Dy and Mg–3Er which are not explicitly shown above are presented in Tables 6–8. For adjoining twin pairs, the Schmid factors of both twins are listed with their common Luster–Morris parameter.

6. Discussion

6.1. Strain distribution and shear banding in pure Mg

Pure Mg exhibits a basal-type recrystallization texture (Fig. 3), i.e. most grains adopt a hard orientation with respect to plane strain boundary conditions, rendering basal slip and tension twinning unfavourable. The most conspicuous observation in pure Mg is the accumulation of intense basal slip activity and strain localization during in situ compression, Fig. 4. This strain localization phenomenon is proposed to be the pre-stage of a shear band and is hereafter referred to as “pre-shear band”.

Experimentally, the formation of this pre-shear band was observed to start in conjunction with massive basal slip traces. After the third deformation step tension twins are formed. No compression or secondary twins were observed. Therefore, the concentrated basal slip activity and strain localization seem to be connected to the formation of shear bands. The crystal orientations of the grains inside the shear band and in the non-shear-banded areas in pure Mg were investigated and compared, Fig. 10. The grains away from the pre-shear band have basal orientations while the grains in the region where the shear band formed have their basal poles about 5–10° deviated from the compression direction, creating a slightly more favourable orientation for basal slip.

However, the experimental observations impose several questions: (i) Is the observed intense basal slip activity the source for or a result of (pre-) shear band formation? (ii) What is the impact of the observed slightly off-basal orientation for the formation of shear bands, both before and after the deformation? (iii) Why does continuous softening

occur as a consequence of localised intense basal slip and not, instead, gradual strain hardening?

In order to answer these questions a series of crystal plasticity simulations with a set of different local boundary conditions for the patch considered is conducted. The imposed local tensorial boundary conditions (final deformation gradient tensor (**F**)) are as follows:

$$\begin{pmatrix} * & 0 & 0 \\ 0 & 0.95 & 0 \\ 0 & 0 & 1.0 \end{pmatrix}_{\text{CP1}} \quad \begin{pmatrix} * & * & 0 \\ 0 & 0.95 & 0 \\ 0 & 0 & 1.0 \end{pmatrix}_{\text{CP2}} \quad \begin{pmatrix} * & 0 & 0 \\ 0 & 0.95 & 0 \\ 0 & 0 & * \end{pmatrix}_{\text{CP3}} \quad \begin{pmatrix} * & * & * \\ 0 & 0.95 & * \\ 0 & 0 & * \end{pmatrix}_{\text{CP4}}$$

The symbol * indicates that this specific deformation component is not prescribed but an unconstrained boundary condition is applied for the respective component. Here, it should be noticed again that these are the average boundary conditions for the complete ROI owing to the periodic boundary conditions. The rationale behind using these different local boundary conditions, as discussed below in more detail for the four cases, lies in identifying possible effects associated with local constraint relaxations for the grain cluster under inspection. The justification for this procedure is given by the experience that in the field of grain mechanics the local deformation state inside a sample of macroscopic dimensions can profoundly differ from the macroscopic boundary conditions [9,10,44,45].

In these CP simulations the initial recrystallized microstructure of the Mg specimen, as measured by EBSD, was used as the starting configuration. In a first crystal plasticity simulation run (CP1) pure plane strain compression without allowing in-plane and out-of-plane shear was applied. These simulation conditions are macroscopically comparable to the deformation state in the sheet centre layers of industrially rolled material or – when translated into laboratory scale – channel die compression conditions. The simulated basal slip activity is shown in Fig. 11a. It is clearly visible that no strain localization occurs, but instead high strain gradients at the grain boundaries are formed under these conditions. To confirm the CP simulation result, channel die experiments were performed and,

Table 5b

Deformation transfer at the GB between grains 9 and 10 in Fig. 9. Schmid factor: m_S ; Luster–Morris parameter: m' ; φ is the angle between two plane normals n_A and n_B , and κ the angle between two slip or shear directions b_A and b_B (see Fig. 2); all angles are specified in degrees.

Grain	Euler angles ($\varphi_1, \phi, \varphi_2$)	Slip/twinning systems	m_S	φ	κ	m'
<i>Slip systems in grains 9 and 10</i>						
9	208.7, 84.8, 165.9	(0001)[$\bar{1}$ 2 $\bar{1}$ 0] ^a	0.390			
10	165.3, 80.9, 200.4	(0001)[$\bar{1}$ 2 $\bar{1}$ 0] ^a	0.465			
<i>Twinning induced by slip in grain 10</i>						
9	208.7, 84.8, 165.9	(0001)[$\bar{1}$ 2 $\bar{1}$ 0] ^a	0.465			
10	165.3, 80.9, 200.4	($\bar{1}$ 012)[10 $\bar{1}$ 1]	−0.457	78.0	75.7	0.051
		(01 $\bar{1}$ 2)[0 $\bar{1}$ 11]	−0.443	79.1	69.4	0.067
		(0 $\bar{1}$ 12)[01 $\bar{1}$ 1]	−0.414	42.1	44.7	0.527
		(10 $\bar{1}$ 2)[$\bar{1}$ 011]	−0.452	43.7	35.2	0.591
		($\bar{1}$ 102)[1 $\bar{1}$ 01]	−0.434	86.0	86.1	0.005
		(1 $\bar{1}$ 02)[$\bar{1}$ 101] ^a	−0.400	0.9	5.1	0.996

^a Activated system.

Table 6

Summary of active twins on the observed plane in pure Mg. Schmid factor: m_S ; Luster–Morris parameter: m' .

Grain	m_S	m'
<i>Adjoining twin pairs</i>		
5	−0.313	0.951
3	−0.410	
5	−0.302	0.757
6	−0.447	
9	−0.480	0.967
10	−0.427	
14	−0.463	0.876
15	−0.475	
15	−0.475	0.922
16	−0.484	
Grain		m_S
<i>Twins nucleated from triple junction</i>		
5		−0.313
6		−0.447
7		−0.475

Table 7

Summary of active twins on the observed plane in Mg–3Dy. Schmid factor: m_S ; Luster–Morris parameter: m' .

Grain	m_S	m'
<i>Slip-induced twins</i>		
2	0.395	0.563
4	−0.328	0.735
5	−0.208	0.313
10	−0.400	0.996
20	0.463	0.935
22	0.447	0.815
28	0.398	0.826
34	−0.210	0.285
34'	−0.193	0.608
<i>Adjoining twin pairs</i>		
1	0.275	0.714
2	0.395	
21	0.061	0.766
22	0.447	

Table 8

Summary of active twins on the observed plane in Mg–3Er. Schmid factor: m_S ; Luster–Morris parameter: m' .

Grain	m_S	m'
<i>Twins nucleated from triple junction</i>		
5-1		−0.283
5-2, 3, 4		−0.256
8		−0.338
9		−0.058
34		−0.175
36		−0.116
39		−0.080
40		−0.312
41		−0.326
42		−0.361
44		−0.412
Grain	m_S	m'
<i>Adjoining twin pairs</i>		
15	−0.279	0.618
16	−0.401	
18	−0.236	0.940
19	−0.389	
18'	−0.273	0.940
19'	−0.408	
20	−0.258	0.441
21	−0.421	
30	−0.284	0.492
32	−0.001	
44	−0.412	0.897
45	−0.421	
<i>Slip-induced twins</i>		
2	−0.287	0.761
18	−0.107	0.958
21	−0.421	0.874
22	−0.327	0.867
24	−0.395	0.626
24'	−0.351	0.543
25	−0.408	0.958
37	−0.356	0.711
45	−0.414	0.878

indeed, no shear banding but instead early fracture of the material along the grain boundaries was observed, Fig. 11b. In a second CP simulation (CP2) plane strain

compression allowing in-plane shear in the image plane (F_{12} free) was applied. The results show slightly lower strain gradients at the grain boundaries than under pure plane strain compression conditions but also no strain

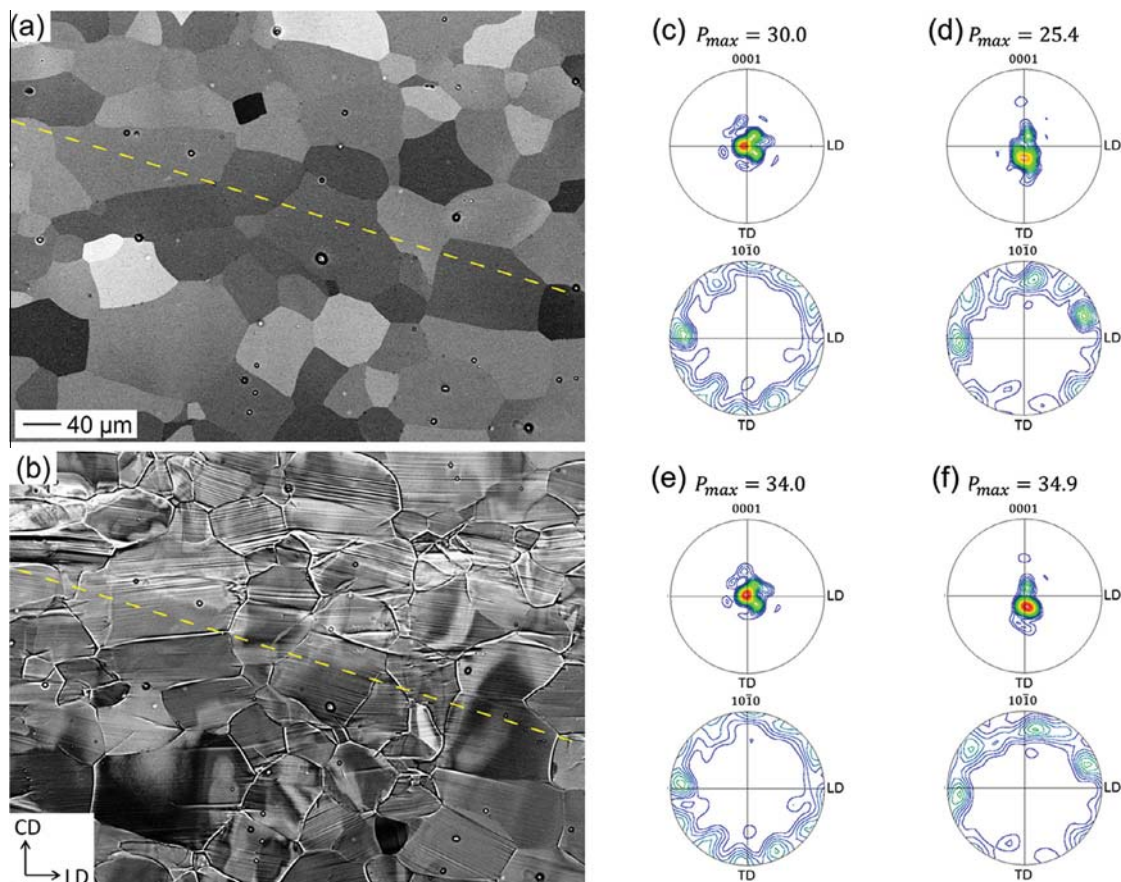


Fig. 10. ECC images and $\{0001\}$, $\{10-10\}$ pole figures of the ROI at (a, c, d) the initial state and (b, e, f) after the fifth compression step. The dashed line divides the ROI into the shear banded region and non-shear-banded region whose respective pole figures are presented in (c–f): (c) non-shear-banded region in the initial state, (d) shear banded region in the initial state, (e) non-shear-banded region after the fifth compression step and (f) shear banded region after the fifth compression step. The fifth deformation step corresponds to $\sim 5\%$ macroscopic strain.

localization occurs. The results indicate that such in-plane shear relaxation is not promoting shear banding and that instead out-of-plane deformation components seem to be required for the formation of shear bands during compression of Mg polycrystals. Therefore, a third CP simulation (CP3) was performed, applying plane strain compression and allowing out-of-plane deformation normal to the image plane (F_{33} free), Fig. 11c. The modelling results show a percolation of high basal slip activity in the upper region of the ROI, Fig. 11c, in agreement with the experimentally observed localised basal activity and shear band formation, Fig. 4f. For a better visualisation the experimental ECCI micrograph (Fig. 4f) and the CP3 basal slip intensity map are superimposed, Fig. 11d. The results imply the subsequent development of a considerable out-of-plane shear stress component during compression. In order to further analyse the impact of this shear stress component, a fourth crystal plasticity simulation was performed, imposing compression loading and allowing additional out-of-plane shear (F_{12} , F_{13} , F_{23} , F_{33} free). The simulation results do not show a significant difference to CP3. These findings imply that the out-of-plane shear stress component which is activated through the percolation of intense basal

dislocation slip in slightly off-basal oriented grains is causing a dynamic facilitating local softening and leading to the formation of shear bands in polycrystalline Mg with pronounced basal texture.

Based on the above presented and discussed experimental and computational results we propose the following mechanisms for shear band formation in basal-textured Mg. A cluster of slightly off-basal oriented grains (where the slightly inclined near-basal texture components might be retained from a preceding inhomogeneous hot working and/or rotation recrystallization step [57–59]) exhibit a slightly more favourable orientation for basal slip than exactly basal oriented grains. In these grains, intensive basal slip is locally activated during the on-set of plastic deformation, leading to a micromechanical strain percolation effect in the form of a collective grain cluster deformation mechanism. This cumulated basal slip extending across multiple neighbored grains creates a pronounced shear component parallel to the active basal glide planes (out-of-plane) in the percolation area and, consequently, basal slip becomes more favourable in this area. Via this dynamical process strain localization is facilitated and results in shear band formation.

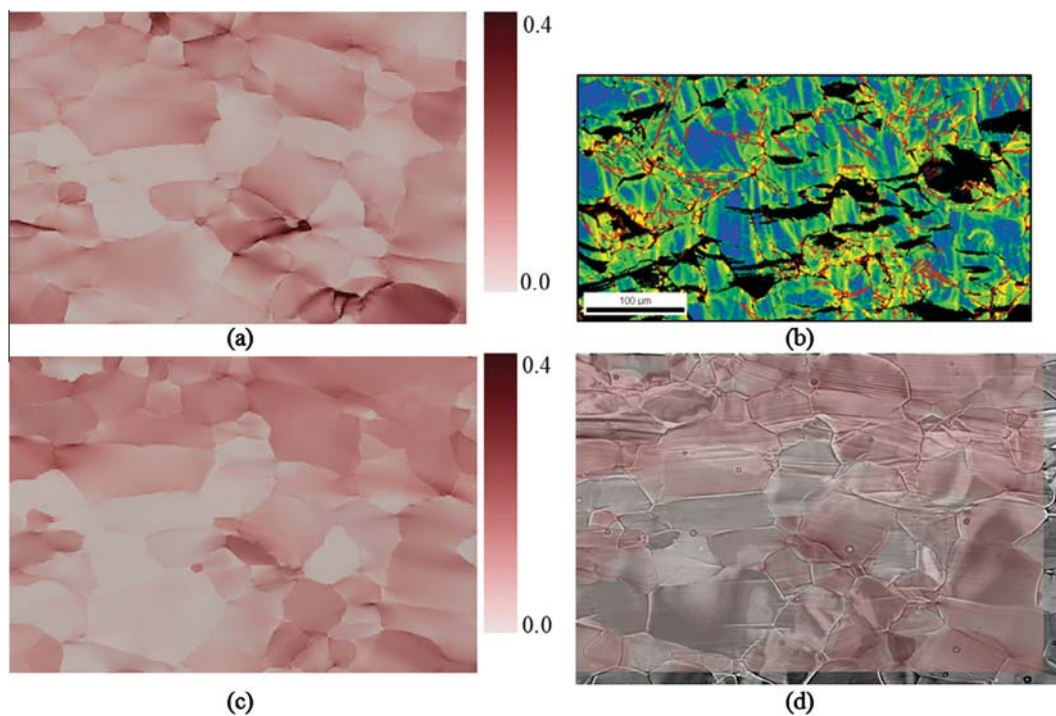


Fig. 11. (a, c) Crystal plasticity simulations using a spectral full field solver; the colour code shows the accumulated basal slip when applying (a) plane strain compression (CP1); (c) plane strain compression allowing out-of-plane shear (CP3); (b) channel die experiment corresponding to CP1 (a); (e) ECCI micrograph after the fifth compression step (see Fig. 2) overlaid with the CP3 map. All simulations and experiments are for pure Mg. For the CP simulations in (a) and (c) the initial recrystallization microstructure of the pure Mg compression sample (Fig. 2) was used as starting configuration.

This proposed mechanism can also be adapted to purely basal oriented material: along the geometrically induced stress concentrations under external load the local stress in the microstructure becomes probably high enough to activate basal dislocation slip. Once the basal slip is activated in one of the grains, pile-ups and stress concentration effects parallel to the active basal planes will occur at its grain boundaries, and hence basal dislocation slip is triggered in the neighbouring grains. Thus, a cluster of grains with basal dislocation slip inducing a shear component parallel to the active basal glide planes develops and the proposed process continues as described above for off-basal tilted grains.

6.2. Activation of tension twinning and variant selection

The above presented analysis of tension twinning reveals that the activation of tension twin variants with (i) high Schmid factor and high Luster–Morris parameter; (ii) high Luster–Morris parameter and low Schmid factor; (iii) high Luster–Morris parameter and negative Schmid factor (in part with high absolute values) can all occur. Many activated twin variants possess negative Schmid factor values. The negative values suggest that the strain produced by tension twinning is opposite to the macroscopic compression strain. This is not surprising in pure Mg considering its intense basal texture where the crystal c -axes of most grains are roughly parallel to the compression direction. In contrast, Mg–3Dy and Mg–3Er possess

more random basal-type textures yet some active tension twins still exhibit a non-Schmid behaviour (Tables 5a, 7 and 8) while others have both a high absolute Schmid factor value and a high Luster–Morris parameter (Tables 4, 5b, 7 and 8). To further analyse the activation of tension twinning in Mg–Er and Mg–Dy, the orientations of grains in which twinning occurred during compression and grains in which no twinning was observed are separately plotted in pole figures, Fig. 12. It should be noticed that only those grains in the ROI where tension twins were identified and those grains in the ROI where no twinning was observed are selected for the plotted pole figures; hence, they do not represent the global textures. In Mg–3Dy, the twinned grains (Fig. 12a) have their c -axes shifted away from the compression direction. The first and second strongest orientation peaks of $\{0001\}$ poles are at 63° and 81° , respectively, with respect to the pole figure centre. When grains of these orientations are subjected to a compression stress, extension along the c -axis is expected and can be realised by the formation of tension twins. In these grains twins with positive and high Schmid factors were observed in Mg–3Dy (Tables 5a, 5b and 7). Contrarily, in Mg–3Er a higher fraction of tension twin variants with lower Schmid factor values and negative Schmid factors (most with high absolute values) was observed (Table 8). In Mg–3Er the twinned grains (Fig. 12c) have their c -axes less shifted away from the compression direction when compared to their counterparts in Mg–3Dy. The peak positions in the $\{0001\}$ pole figure are at 25° and 51° , respectively, with

respect to the pole figure centre. The effect of the global compression strain on these grains is contraction along the *c*-axis.

The orientations of the grains in the ROI demonstrate that tension twinning occurs preferentially in the grains with larger deviations of the basal poles from the compression direction although the orientation may still be unfavourable for the activation of tension twinning due to their negative Schmid factors.

In pure Mg, twinning occurs in hard oriented grains inside the pre-shear band after intense basal slip activity. Due to strain localization it is very likely that the local stress state is different from the global stress state, in both, magnitude and directionality. Regardless of the Schmid factor value, adjoining twin pairs possess quite high values of the Luster–Morris parameter (Table 6).

In Mg–3Dy there are variants activated with both the highest Schmid factor and Luster–Morris values among six variants, e.g. in grains 1, 21, 22, but also variants with low and/or negative Schmid factors but the highest Luster–Morris values, e.g. in grains 4 and 10 (see Table 7). In Mg–3Er all observed twin variants have negative Schmid factors, several of them with high absolute values and high Luster–Morris parameters. Depending on the deformation modes in the adjacent grain, different variants are activated from the GB to fulfil the respective geometric compatibility.

For twinning-induced tension twins the analysis shows that the tension twin which was first activated generally is characterised by a high Schmid factor value while the second activated twin, i.e. the twin-stimulated twin, possesses always a high Luster–Morris parameter, but in most cases not the highest Schmid factor value. This indicates

again that lower Schmid factor tension twins are activated in unfavourably oriented grains to accommodate the local strain and maintain strain compatibility.

Since the tension twin variants with a high Luster–Morris parameter and a high absolute Schmid factor value prevail in general, it is concluded from the present observation that besides the Schmid factor the strain transfer compatibility plays an important role in twin nucleation. The cases where Schmid's law of tension twinning was not fulfilled are probably resulting from the unfavourable orientation of grains rather than a reflection of the nature of twin activation. In fact, if the material is strained in a favourable orientation, e.g. compression along the RD and tension along the ND in rolled material [60], or compression along the extrusion direction and tension along the tangential direction in extruded material [61], good agreement with Schmid's law is observed.

Direct comparison between pure Mg and the Mg–RE alloys shows that in pure Mg localised and higher basal slip activity and a lower tension twin activity than in Mg–Er and Mg–Dy was observed. In both Mg–RE alloys no localised deformation was observed; the activation of tension twins occurred slightly later and twin propagation was found to be slightly faster than in pure Mg. The distribution of tension twins was homogeneous in Mg–Er and Mg–Dy, whereas in pure Mg tension twins were observed to nucleate in the area of localised strain. Compression and secondary twins were observed in both Mg–RE alloys only at higher strains in ex situ experiments. The observed differences in tension twinning between pure Mg and Mg–RE are assumed to result from texture effects. In the present work, the pure Mg sample possesses a stronger

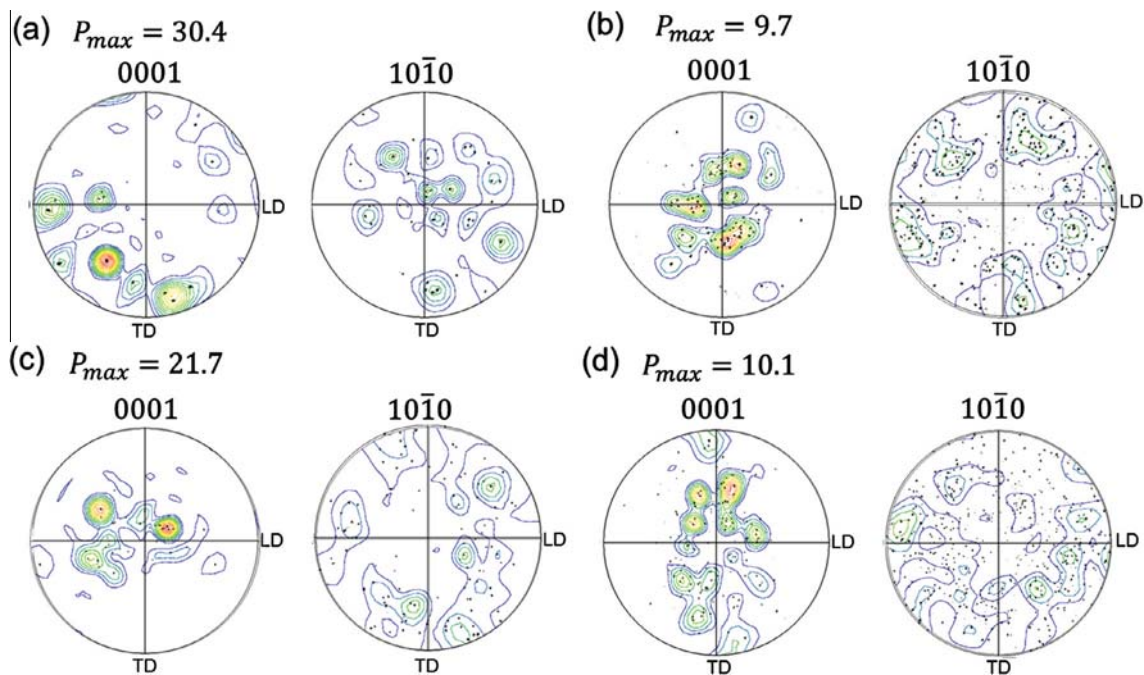


Fig. 12. Pole figures based on orientation data of grains in which twins develop in subsequent compression (a, c) and grains in which no twin is observed during the test (b, d) in the ROI of Mg–3Dy after the first compression step (a, b) and of Mg–3Er after the second compression step (c, d). Each compression step corresponds to $\sim 1\%$ engineering strain.

and the two Mg–RE alloys weaker basal-type textures; therefore it can be assumed that the Schmid and non-Schmid behaviour of tension twins is firstly affected by the texture. During the early stages of compressive deformation no “RE-effect” other than RE-induced texture weakening on the activation of tension twinning was observed.

In summary, the formation of tension twinning is rationalised in the following way. For grains with an orientation where the compressive stress component is parallel to the basal plane or the tensile stress component along the crystal *c*-axis, tension twinning is favoured. Here, the twin variant which is geometrically well aligned with the deformation mode in the adjacent grain is preferentially activated. For grains with orientations that render tension twinning unfavourable, due to their hard orientation for twinning, the global strain cannot be effectively accommodated and stress concentrates at grain boundaries. When the concentrated stress is high enough to activate twinning, and if there is a geometrically well-aligned deformation mode in the adjacent grain, it is activated. Otherwise, strong strain gradients form in the vicinity of the GB, as is manifested by local orientation variations or even ledges at the GB, such as observed in pure Mg (Fig. 4). Besides the Schmid factor several other factors seem to contribute to the twin variant selection in Mg alloys: (i) strain accommodation required by the neighbouring grains [22], GB character and misorientation [30], (iii) minimization of compatibility strain in the case of secondary twinning [24] and (iv) strain compatibility across grain boundaries as analysed in the present study.

7. Conclusions

We analysed by in situ deformation the microstructure development of pure Mg and two Mg–RE alloys (Mg–3%Dy and Mg–3%Er) at the grain scale. The main observations and conclusions are as follows:

- (1) Below an engineering strain of 5%, pure Mg exhibits localised slip activity, causing the formation of a pre-shear band and twinning exclusively in this pre-shear band. In contrast, the two Mg–RE alloys exhibit homogeneous deformation and a larger contribution of activated tension twins. The basal texture and the associated grain clusters of similar basal orientation in the recrystallized pure Mg are an important factor responsible for strain localization.
- (2) During the early stages of compressive deformation no “RE-effect” other than RE-induced texture weakening on the activation of tension twinning was observed.
- (3) Combined in situ deformation experiments and crystal plasticity simulations indicate that strain localization and pre-shear band formation in pure Mg is a result of percolated basal slip activity in slightly off-basal orientated grains. As a result of this locally

accumulated intense basal slip a shear stress component parallel to the active basal glide planes develops and subsequently eases the basal slip, leading to the formation of a pre-shear band.

- (4) Non-Schmid behaviour of tension twinning was observed in both pure Mg and the two Mg–RE alloys. However, it appears in the two Mg–RE alloys that activation of tension twinning preferentially occurs in grains showing a larger deviation between the crystal *c*-axis and the compression direction. In pure Mg, tension twins are activated in areas with high local stresses, i.e. inside shear bands.
- (5) The Luster–Morris parameter describes the geometric compatibility and is an effective criterion in variant selection for twin activation. The activation of tension twinning can be understood in combination with the local stress tensor only. Analysis of the Luster–Morris parameter and the (global) Schmid factor of activated tension twins revealed that twinning follows Schmid’s law in orientations favourable for twinning, while in orientations where twinning is not favoured by the macroscopic stress state twinning is more a process of accommodating local strain and thereby maintaining strain compatibility at grain boundaries than a response to macroscopically imposed strain in Mg and Mg alloys at low strain levels.

Acknowledgments

Parts of this research (CP simulations) were carried out under project number M 41.2.10410 in the framework of the research program of the Materials innovation institute M2i (www.m2i.nl).

References

- [1] ASM Handbook. Properties and selections: nonferrous alloys and special purpose materials, vol. 2. Materials Park, OH: ASM; 1991.
- [2] Schumann S, Friedrich H. *Mater Sci Forum* 2003;419–422:51–6.
- [3] Yoo M. *Metall Trans A* 1981;12:409–18.
- [4] Akhtar A, Teghtsoonian E. *Acta Metall* 1969;17:1339–49.
- [5] Hatherly M, Humphreys FJ. *Recrystallization and related annealing phenomena*. Oxford: Elsevier; 1996.
- [6] Gottstein G, Al Samman T. *Mater Sci Forum* 2005;495–497:623–32.
- [7] Agnew S, Yoo M, Tomé C. *Acta Mater* 2001;49(20):4277–89.
- [8] Bishop JFW, Hill R. *Philos Mag* 1951;42:414–27.
- [9] Raabe D, Sachtleber M, Zhao Z, Roters F, Zaefferer S. *Acta Mater* 2001;49:3433–41.
- [10] Zhao Z, Ramesh M, Raabe D, Cuitino A, Radovitzky R. *Int J Plast* 2008;24:2278–97.
- [11] Jia N, Roters F, Eisenlohr P, Kords C, Raabe D. *Acta Mater* 2012;60:1099–115.
- [12] Scott J, Miles M, Fullwood D, Adams B, Khosravani A, Mishra RK. *Metall Mater Trans A* 2013;44:512–6.
- [13] Hazeli K, Cuadra J, Vanniamparambil PA, Kontsos A. *Scripta Mater* 2013;68:83–6.
- [14] Kim HL, Lee J-H, Lee CS, Bang W, Ahn SH, Chang YW. *Mater Sci Eng A* 2012;558:431–8.
- [15] Chun YB, Davies CHJ. *Mater Sci Eng A* 2012;556:253–9.

- [16] Zhang Z, Wang M-P, Jiang N, Zhu S. *J Alloys Compd* 2012;512:73–8.
- [17] Ion S, Humphreys F, White S. *Acta Metall* 1982;30:1909–19.
- [18] Barnett M, Nave M, Bettles C. *Mater Sci Eng A* 2004;386:205–11.
- [19] Koike J, Sato Y, Ando D. *Mater Trans* 2008;49:2792–800.
- [20] Jiang J, Godfrey A, Liu W, Liu Q. *Scripta Mater* 2008;58:122–5.
- [21] Beyerlein IJ, Capolungo L, Marshall PE, McCabe RJ, Tomé C. *Philos Mag* 2010;90:2161–90.
- [22] Jonas JJ, Mu S, Al-Samman T, Gottstein G, Jiang L, Martin E. *Acta Mater* 2011;59:2046–56.
- [23] Agnew S, Tomé C, Brown D, Holden T, Vogel S. *Scripta Mater* 2003;48:1003–8.
- [24] Barnett M, Keshavarz Z, Beer A, Atwell D. *Acta Mater* 2004;52:5093–103.
- [25] Wang L, Eisenlohr P, Yang Y, Bieler T, Crimp M. *Scripta Mater* 2010;63:827–30. 87 Bibliography 88.
- [26] Wang L, Yang Y, Eisenlohr P, Bieler T, Crimp M, Mason D. *Metall Mater Trans A* 2010;41:421–30.
- [27] Mu S, Jonas JJ, Gottstein G. *Acta Mater* 2012;60:2043–53.
- [28] Capolungo L, Marshall P, McCabe R, Beyerlein I, Tomé C. *Acta Mater* 2009;57:6047–56.
- [29] Christian J, Mahajan S. *Prog Mater Sci* 1995;39:1–157.
- [30] El Kadiri H, Baird JC, Kapil J, Oppedal AL, Cherkaoui M, Vogel SC. *Int J Plast* 2013;44:111–20.
- [31] Mishra RK, Gupta AK, Rao PR, Sachdev AK, Kumar AM, Luo AA. *Scripta Mater* 2008;59:562–5.
- [32] Stanford N. *Mater Sci Eng A* 2010;527:2669–77.
- [33] Bohlen J, Nürnberg MR, Senn JW, Letzig D, Agnew SR. *Acta Mater* 2007;55:2101–12.
- [34] Stanford N, Atwell D, Beer A, Davies CHJ, Barnett MR. *Scripta Mater* 2008;59:772–5.
- [35] Bohlen J, Yi S, Letzig D, Kainer KU. *Mater Sci Eng A* 2010;527:7092–8.
- [36] Al-Samman T, Li X. *Mater Sci Eng A* 2011;528:3809–22.
- [37] Sandlöbes S, Zaefferer S, Schestakow I, Yi S, Gonzalez-Martinez R. *Acta Mater* 2011;59:429–39.
- [38] Zaefferer S, Elhami NN. *Acta Mater* 2014;75:20–50.
- [39] Gutierrez-Urrutia I, Zaefferer S, Raabe D. *Scripta Mater* 2009;61:737–40.
- [40] Gutierrez-Urrutia I, Zaefferer S, Raabe D. *JOM* 2013;65:1229–36.
- [41] Bridier F, Vilechaise P, Mendez J. *Acta Mater* 2005;53:555–67.
- [42] Simkin B, Ng B, Bieler T, Crimp M, Mason D. *Intermetallics* 2003;11:215–23.
- [43] Luster J, Morris M. *Metall Mater Trans A* 1995;26:1745–56.
- [44] Bieler T, Eisenlohr P, Roters F, Kumar D, Mason D, Crimp M, et al. *Int J Plast* 2009;25:1655–83.
- [45] Roters F, Eisenlohr P, Hantcherli L, Tjahjanto DD, Bieler TR, Raabe D. *Acta Mater* 2010;58:1152–211.
- [46] Eisenlohr P, Diehl M, Lebensohn RA, Roters F. *Int J Plast* 2013;46:37–53.
- [47] Shanthraj P, Eisenlohr P, Diehl M, Roters F. *Int J Plast*; in press, <http://dx.doi.org/10.1016/j.ijplas.2014.02.006>.
- [48] Hutchinson JW. *Proc R Soc Lond A* 1976;348:101–27.
- [49] Roters F. Advanced material models for the crystal plasticity finite element method – development of a general CPFEM framework. RWTH Aachen, Aachen; 2011. URL: <http://darwin.bth.rwth-aachen.de/opus3/volltexte/2011/3874/>.
- [50] Roters F, Eisenlohr P, Kords C, Tjahjanto DD, Diehl M, Raabe D. *Procedia IUTAM* 2012;3:3–10.
- [51] DAMASK, Düsseldorf Advanced Material Simulation Kit, <http://damask.mpie.de/>.
- [52] Prakash A, Weygand SM, Riedel H. *Comput Mater Sci* 2009;45:744–50.
- [53] Kalidindi SR. *J Mech Phys Solids* 1998;48:267–90.
- [54] Tromans D. *Int J Res Rev Appl Sci* 2011;6(4):462–83.
- [55] Agnew S, Brown D, Tomé CN. *Acta Mater* 2006;54(18):4841–52.
- [56] Beyerlein I, McCabe R, Tomé C. *J Mech Phys Solids* 2011;59:988–1003.
- [57] Ion SE, Humphreys FJ, White SH. *Acta Metall* 1982;30:1909–19.
- [58] Cottam R, Robson J, Lorimer G, Davis B. *Mater Sci Eng A* 2008;485:375–82.
- [59] Yi SB, Zaefferer S, Brokmeier H-G. *Mater Sci Eng A* 2006;424:275–81.
- [60] Park SH, Hong S-G, Lee CS. *Scripta Mater* 2010;62:202–5.
- [61] Godet S, Jiang L, Luo A, Jonas J. *Scripta Mater* 2006;55:1055–8.